Energy difference between hodoscope sections in muon tomography: Application for nuclear waste barrels by means of GEANT4 simulations

Ahmet Ilker Topuz[1], Madis Kiisk[1], and Andrea Giammanco[2]

[1]University of Tartu
[2]Université catholique de Louvain

January 20, 2023

Abstract

The propagating muons deposit their energies in the volume-of-interest (VOI) within the tomographic configurations, and this energy loss directly indicates that there is a difference in terms of the kinetic energy between the incoming muons and the the outgoing muons. In this study, by using the GEANT4 simulations, we first elaborate this energy difference over the nuclear waste barrels that contain cobalt, strontium, caesium, uranium, and plutonium. We show that the deposited energy through these VOIs is not negligible for the initial energy bins. Then, we suggest a correction factor for the image reconstruction codes where the initial kinetic energy of the entering muons is coarsely predicted in accordance with the deflection angle through the hodoscope sections, thereby renormalizing the deflection angle in the bottom hodoscope depending on the intrinsic properties of the corresponding VOIs. This correction factor encompasses useful information about the target volume traversed by the muons since it is related to the intrinsic features of the VOI. Therefore, it might be utilized in order to complement the scattering information as an input to the image reconstruction.

Energy difference between hodoscope sections in muon tomography: Application for nuclear waste barrels by means of GEANT4 simulations

A. Ilker Topuz[1,2], Madis Kiisk[1,3], Andrea Giammanco[2]

[1]Institute of Physics, University of Tartu, W. Ostwaldi 1, 50411, Tartu, Estonia
[2]Centre for Cosmology, Particle Physics and Phenomenology, Université catholique de Louvain,
Chemin du Cyclotron 2, B-1348 Louvain-la-Neuve, Belgium
[3]GScan OU, Maealuse 2/1, 12618 Tallinn, Estonia

Abstract

The propagating muons deposit their energies in the volume-of-interest (VOI) within the tomographic configurations, and this energy loss directly indicates that there is a difference in terms of the kinetic energy between the incoming muons and the the outgoing muons. In this study, by using the GEANT4 simulations, we first elaborate this energy difference over the nuclear waste barrels that contain cobalt, strontium, caesium, uranium, and plutonium. We show that the deposited energy through these VOIs is not negligible for the initial energy bins. Then, we suggest a correction factor for the image reconstruction codes where the initial kinetic energy of the entering muons is coarsely predicted in accordance with the deflection angle through the hodoscope sections, thereby renormalizing the deflection angle in the bottom hodoscope depending on the intrinsic properties of the corresponding VOIs. This correction factor encompasses useful information about the target volume traversed by the muons since it is related to the intrinsic features of the VOI. Therefore, it might be utilized in order to complement the scattering information as an input to the image reconstruction.

1   Introduction

The traversing muons lose their energies [1, 2] through the volume-of-interest (VOI) in the tomographic setups based on the muon scattering [3, 4]. This energy loss is not frequently mentioned because most of the tomographic configurations do not have a custom spectrometer to track the kinetic energy of the propagating muons. However, the deflection angle through the hodoscope section might be used to roughly estimate the kinetic energy of the entering muons as described in another study [5, 6]. In this study, we explore the energy loss of the incoming muons through the VOIs over the nuclear waste barrels [7–13] that include cobalt, caesium, strontium, uranium, and plutonium by means of the GEANT4 simulations [14]. Then, we propose a correction factor for the image reconstruction codes that coarsely group the entering muons according to the deflection angle through the hodoscope sections. The present study is organized as follows. In section 2, we state our methodology in order to determine the energy difference between the hodoscope sections. While we mention our simulation setup as well our

simulation features in section 3, we exhibit our simulation outcomes in section 4. We suggest our correction factor for the image reconstruction codes that are founded on the deflection angle in section 5 and we draw our conclusions in section 6.

2 Methodology

We start with illustrating our tomographic setup that is given in Fig. 1, and the energy values are collected at the top hodoscope section above the VOI as well as the bottom hodoscope section below the VOI as indicated by the red circle and the green circle, respectively.
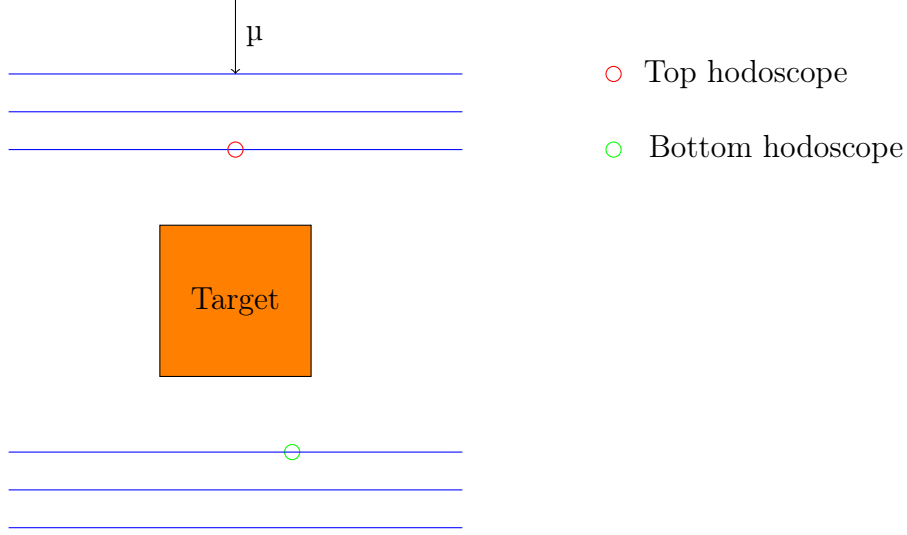

Figure 1: Tomographic setup for the collection of energy values.

The energy difference between the hodoscope sections depicted in Fig. 1 is determined by using the following expression:

$$\Delta E = E_{\text{Top}} - E_{\text{Bottom}} \tag{1}$$

where E_{Top} is the kinetic energy that is registered in the third top detector layer before the target volume, and E_{Bottom} is the kinetic energy that is tracked in the first bottom detector layer after the target volume. Since a substantial number of muons reach the VOI, the average energy difference at a certain energy bin is determined by averaging the previously determined energy differences over N number of the non-absorbed/non-decayed muons as written in

$$\overline{\Delta E} = \frac{1}{N} \sum_{i=1}^{N} \Delta E_i \tag{2}$$

where its standard deviation is

$$\delta \Delta E = \sqrt{\frac{1}{N} \sum_{i=1}^{N} (\Delta E_i - \overline{\Delta E})^2} \tag{3}$$

3 Simulation properties

To perform the aforementioned analysis for the nuclear waste barrels, the geometrical scheme is depicted in Fig. 2, and it is shown that the plastic scintillators are separated by a distance

of 10 cm, whereas the distance between these two hodoscope sections is 100 cm. Furthermore, the dimensions of the detector layers are $100 \times 0.4 \times 100$ cm^3. Concerning the nuclear waste drum, the VOI is held at the center of the tomographic system. Regarding the components of the nuclear waste barrel, the outermost layer is defined as a cylinder manufactured from stainless steel layer, the height of which is 96 cm, and the thickness of which is 3.2 cm. The filling material is the cylindrical ordinary concrete slab with the height of 88 cm as well as the radius of 26.2 cm, while the nuclear material placed at the middle of the concrete padding is a cubic solid box of $20 \times 20 \times 20$ cm^3.
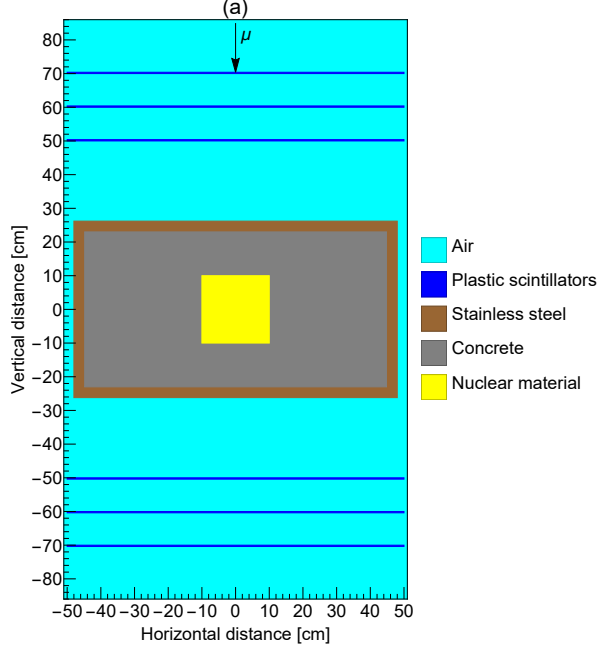

Figure 2: Simulation setup.

By satisfying the geometrical properties of the tomographic setup as well as the regular nuclear waste drum, we conduct the Monte Carlo simulations via the GEANT4 code in order to register the energy values in the plastic scintillators. The simulation parameters are listed in Table 1, and the dimension of the simulation box is $100 \times 170 \times 100$ cm^3 where the Cartesian components are situated symmetrically in the interval of (-50 cm, 50 cm), (-85 cm, 85 cm), and (-50 cm, 50 cm), respectively as indicated in Fig. 2. We use a narrow planar multi-energetic mono-directional beam that is generated at ([-0.5, 0.5] cm, 85 cm, [-0.5, 0.5] cm) via G4ParticleGun, and the generated muons are propagating in the vertically downward direction as shown by the black arrow in Fig. 2, i.e. from the top edge of the simulation box through the bottom edge.

A uniform energy distribution lying on the interval between 0 and 8 GeV with the energy cut-off of 0.1 GeV, which is selected to minimize the probability of the muon absorption in the top detector layers as well as to maximize the encounter between the incoming muons and the VOI, is utilized by recalling the numerical advantages [15]. The total number of the generated μ^- is 10^5 in every simulation. All the materials in the simulation geometry are defined in agreement with the GEANT4/NIST material database, and FTFP_BERT is the reference physics list used in the present study.

Table 1: Simulation properties.

Particle	μ^-
Beam direction	Vertical
Momentum direction	(0, -1, 0)
Source geometry	Planar
Initial position (cm)	([-0.5, 0.5], 85, [-0.5, 0.5])
Number of particles	100,000
Energy interval (GeV)	[0, 8]
Energy cut-off (GeV)	0.1
Bin step length (GeV)	0.5
Energy distribution	Uniform
Material database	G4/NIST
Reference physics list	FTFP_BERT

The muon tracking is maintained by G4Step, and the registered energy values are post-processed by the aid of a Python script where the energy difference is first calculated for every single non-absorbed/non-decayed muon, then the uniform energy spectrum bounded by 0 and 8 GeV is partitioned into 16 bins by marching with a step of 0.5 GeV, and each obtained energy bin is labeled with the central point in the energy sub-interval. Consequently, the obtained energy differences are averaged for the associated energy bins.

4 Simulation results

We exhibit our simulation outcomes in Table 2 and we initially show that the energy loss is a characteristic parameter that is dependent on the intrinsic properties of the VOIs. While the waste barrels containing uranium and plutonium yields the highest deposited energy, the reference barrel indicated by WB, which only includes stainless steel and concrete, leads to the lowest energy loss.

Table 2: Energy difference between hodoscope sections and their corresponding standard deviations for the nuclear waste barrels over the energy interval between 0.1 and 8 GeV.

$\bar{E}$ [GeV]	$\overline{\Delta E}_{\mathrm{WB}} \pm \delta\Delta E$ [GeV]	$\overline{\Delta E}_{\mathrm{WB+Co}} \pm \delta\Delta E$ [GeV]	$\overline{\Delta E}_{\mathrm{WB+Sr}} \pm \delta\Delta E$ [GeV]	$\overline{\Delta E}_{\mathrm{WB+Cs}} \pm \delta\Delta E$ [GeV]	$\overline{\Delta E}_{\mathrm{WB+U}} \pm \delta\Delta E$ [GeV]	$\overline{\Delta E}_{\mathrm{WB+Pu}} \pm \delta\Delta E$ [GeV]
0.75	0.291±0.018	0.470±0.021	0.283±0.018	0.261±0.017	0.648±0.026	0.664±0.026
1.25	0.307±0.029	0.495±0.034	0.300±0.028	0.276±0.028	0.678±0.039	0.695±0.039
1.75	0.317±0.040	0.516±0.050	0.310±0.043	0.286±0.038	0.713±0.057	0.731±0.061
2.25	0.325±0.050	0.530±0.062	0.317±0.050	0.292±0.050	0.739±0.076	0.755±0.077
2.75	0.330±0.064	0.541±0.077	0.323±0.058	0.299±0.057	0.758±0.099	0.776±0.092
3.25	0.335±0.076	0.550±0.092	0.331±0.074	0.304±0.073	0.774±0.116	0.793±0.113
3.75	0.341±0.095	0.558±0.108	0.333±0.076	0.308±0.088	0.787±0.134	0.805±0.127
4.25	0.342±0.085	0.564±0.118	0.337±0.105	0.311±0.095	0.800±0.160	0.819±0.175
4.75	0.345±0.106	0.571±0.128	0.342±0.119	0.314±0.091	0.810±0.174	0.833±0.176
5.25	0.349±0.112	0.575±0.142	0.342±0.118	0.316±0.107	0.813±0.183	0.835±0.193
5.75	0.354±0.133	0.579±0.155	0.347±0.118	0.320±0.123	0.824±0.202	0.850±0.231
6.25	0.353±0.126	0.584±0.169	0.347±0.123	0.321±0.144	0.831±0.218	0.855±0.223
6.75	0.354±0.132	0.591±0.186	0.352±0.165	0.321±0.130	0.840±0.255	0.867±0.265
7.25	0.360±0.155	0.593±0.193	0.356±0.183	0.326±0.150	0.849±0.295	0.865±0.256
7.75	0.359±0.147	0.598±0.221	0.357±0.175	0.330±0.162	0.851±0.278	0.879±0.293

According to the listed values in Table 2, the energy loss is not negligible for the first few energy bins. This also means that the scattering regime for the initial energy bins changes significantly after the VOIs, and this may necessitate a correction factor for the image reconstruction codes where the kinetic energy of the incoming muons is coarsely estimated according to the deflection angle in the top hodoscope and the bottom hodoscope since the deflection angle is contingent on the kinetic energy of the crossing muons. In order to highlight the spectral difference between two hodoscope sections, Fig. 3 shows the energy distributions at either section.
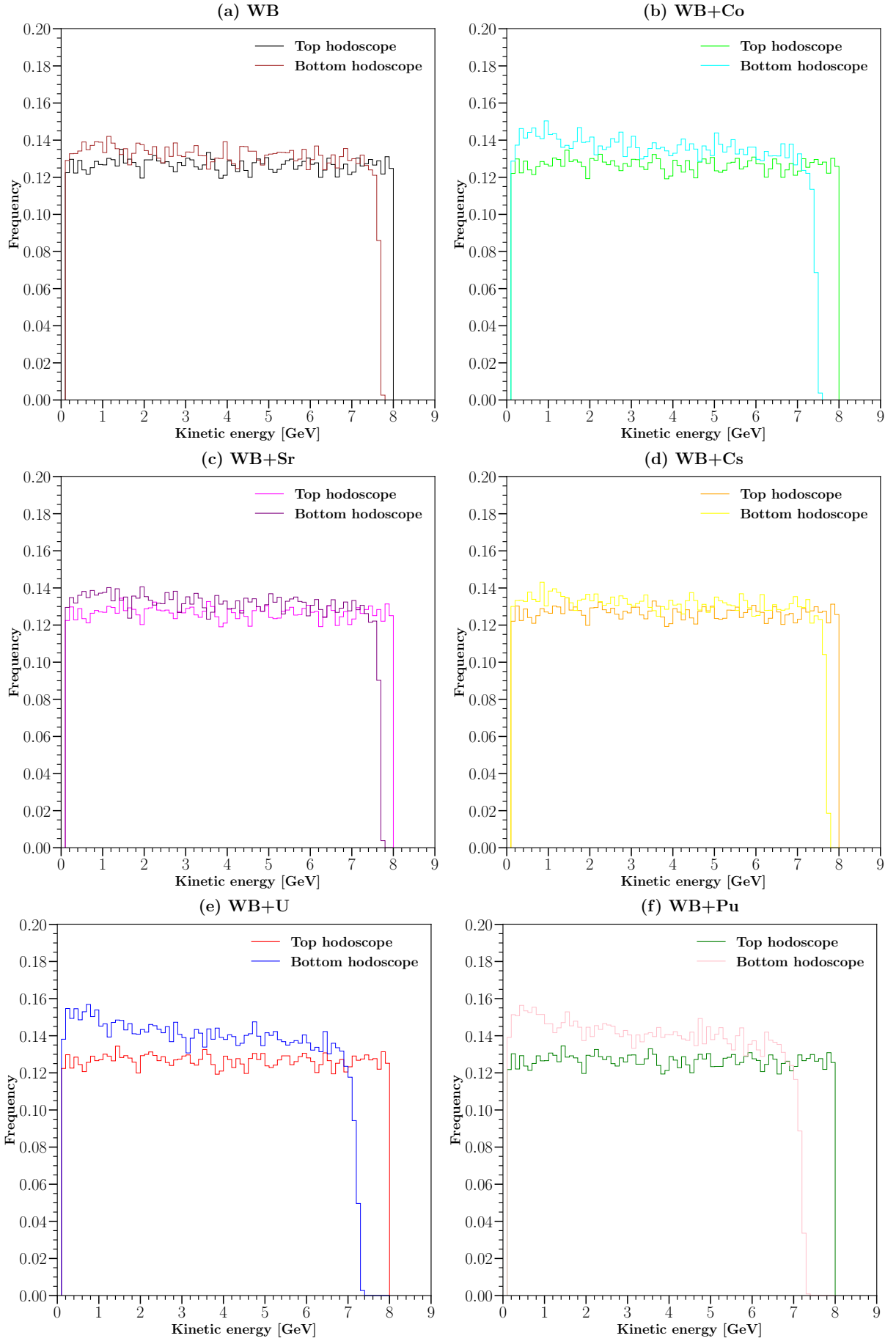
Figure 3: Spectral difference between hodoscope sections for nuclear waste barrels over the energy interval between 0.1 and 8 GeV.

5 Correction factor for image reconstruction

As described in another study [5, 6], the kinetic energy of the incoming muons might be estimated by using the deflection angle at the hodoscope sections. Moreover, the deflection angles obtained through these hodoscope sections are averaged in order to decrease the resulting standard deviation. According to Table 2 and Fig. 3, it is shown that the energy values of the incoming muons are different from those of the outgoing muons in the presence of the VOIs, and the deflection angle at the bottom section varies depending on the intrinsic properties of the VOIs. Thus, it is necessary to renormalize the bottom deflection angle for the image reconstruction purposes. The distribution of the deflection angle as function of momentum is described in the following expression:

$$\theta \approx \frac{13.6 \text{ MeV}}{\beta p}\sqrt{\frac{l}{X_0}} \tag{4}$$

where p is the momentum, β is the velocity, l is the thickness of the material, and X_0 is the radiation length of the material. Then, by assuming that the top hodoscope and the bottom hodoscope are completely symmetrical and made out of the same materials as shown in Figs. 1 and 3,

$$\frac{\theta_{\text{Top}}}{\theta_{\text{Bottom}}} \approx \frac{\frac{13.6 \text{ MeV}}{\beta_{\text{Top}}p_{\text{Top}}}\sqrt{\frac{l}{X_0}}}{\frac{13.6 \text{ MeV}}{\beta_{\text{Bottom}}p_{\text{Bottom}}}\sqrt{\frac{l}{X_0}}} = \frac{\beta_{\text{Bottom}}p_{\text{Bottom}}}{\beta_{\text{Top}}p_{\text{Top}}} \approx \frac{E_{\text{Bottom}}}{E_{\text{Top}}} \tag{5}$$

So, a correction factor for the bottom hodoscope might be formulated as

$$C = \frac{\bar{\theta}_{\text{Top}}}{\bar{\theta}_{\text{Bottom}}} \tag{6}$$

This correction factor might be useful for the image reconstruction codes where the kinetic energy of the entering muons is roughly predicted according to the deflection angle.

6 Conclusion

In this study, we compute the energy difference between the hodoscope sections in the presence of the nuclear waste barrels and we show that the energy loss is a non-negligible characteristic parameter that varies in accordance with the intrinsic properties of the target volumes. For the image reconstruction codes where the kinetic energy of the incoming muons is coarsely determined by using the the deflection angle, we emphasize the necessity of a correction factor that renormalizes the bottom deflection affected by the corresponding VOIs. By aiming at characterizing the target volume, this correction factor might be used to provide complementary details in addition to the scattering information in the course of the image reconstruction.

References

[1] D. E. Groom, N. V. Mokhov, S. I. Striganov, Muon stopping power and range tables 10 MeV–100 TeV, Atomic Data and Nuclear Data Tables 78 (2) (2001) 183–356.

[2] P. Zyla, et al., Review of Particle Physics, PTEP 2020 (8) (2020) 083C01. `doi:10.1093/ptep/ptaa104`.

[3] S. Procureur, Muon imaging: Principles, technologies and applications, Nuclear Instruments and Methods in Physics Research Section A: Accelerators, Spectrometers, Detectors and Associated Equipment 878 (2018) 169–179.

[4] L. Bonechi, R. D'Alessandro, A. Giammanco, Atmospheric muons as an imaging tool, Reviews in Physics 5 (2020) 100038.

[5] A. I. Topuz, M. Kiisk, A. Giammanco, M. Mägi, On muon energy group structure based on deflection angle for application in muon scattering tomography: A Monte Carlo study through GEANT4 simulations, RAP Conference Proceedings, 2021, pp. 27–31. `doi:10.37392/RapProc.2021.06.`

[6] A. I. Topuz, M. Kiisk, A. Giammanco, M. Mägi, Effect of passive metallic layers on muon energy estimation by means of deflection angle for muon scattering tomography: a comparative study based on GEANT4 simulations, Journal of Instrumentation 17 (02) (2022) C02008.

[7] D. Mahon, A. Clarkson, D. Hamilton, M. Hoek, D. Ireland, J. Johnstone, R. Kaiser, T. Keri, S. Lumsden, B. McKinnon, et al., A prototype scintillating-fibre tracker for the cosmic-ray muon tomography of legacy nuclear waste containers, Nuclear Instruments and Methods in Physics Research Section A: Accelerators, Spectrometers, Detectors and Associated Equipment 732 (2013) 408–411.

[8] A. Clarkson, D. J. Hamilton, M. Hoek, D. G. Ireland, J. Johnstone, R. Kaiser, T. Keri, S. Lumsden, D. F. Mahon, B. McKinnon, et al., GEANT4 simulation of a scintillating-fibre tracker for the cosmic-ray muon tomography of legacy nuclear waste containers, Nuclear Instruments and Methods in Physics Research Section A: Accelerators, Spectrometers, Detectors and Associated Equipment 746 (2014) 64–73.

[9] A. Clarkson, D. G. Ireland, R. Al Jebali, R. Kaiser, S. Lumsden, D. Mahon, D. Mountford, M. Ryan, C. Shearer, G. Yang, Characterising encapsulated nuclear waste using cosmic-ray Muon Tomography (MT), in: 2015 4th international conference on Advancements in Nuclear Instrumentation Measurement Methods and their Applications (ANIMMA), IEEE, 2015, pp. 1–7.

[10] C. Thomay, J. Velthuis, T. Poffley, P. Baesso, D. Cussans, L. Frazão, Passive 3D imaging of nuclear waste containers with muon scattering tomography, Journal of Instrumentation 11 (03) (2016) P03008.

[11] L. Frazão, J. Velthuis, S. Maddrell-Mander, C. Thomay, High-resolution imaging of nuclear waste containers with muon scattering tomography, Journal of Instrumentation 14 (08) (2019) P08005.

[12] A. I. Topuz, M. Kiisk, A. Giammanco, Non-destructive interrogation of nuclear waste barrels through muon tomography: A Monte Carlo study based on dual-parameter analysis via GEANT4 simulations, arXiv preprint arXiv:2106.14302 (2021).

[13] A. I. Topuz, M. Kiisk, A. Giammanco, On discrimination of nuclear waste barrels subject to in-drum mixing by muon scattering tomography: A characterization study based on GEANT4 simulations, in: American Chemical Sociecity Spring 2022, ACS, 2022. `doi:10.1021/scimeetings.2c00098.`

[14] S. Agostinelli, et al., GEANT4 - a simulation toolkit, Nuclear instruments and methods in physics research section A: Accelerators, Spectrometers, Detectors and Associated Equipment 506 (3) (2003) 250–303.

[15] V. Anghel, J. Armitage, F. Baig, K. Boniface, K. Boudjemline, J. Bueno, E. Charles, P. Drouin, A. Erlandson, G. Gallant, et al., A plastic scintillator-based muon tomography system with an integrated muon spectrometer, Nuclear Instruments and Methods in Physics Research Section A: Accelerators, Spectrometers, Detectors and Associated Equipment 798 (2015) 12–23.